Atmos. Meas. Tech., 9, 1767–1784, 2016
www.atmos-meas-tech.net/9/1767/2016/
doi:10.5194/amt-9-1767-2016

Atmospheric Measurement Techniques
Open Access
EGU

The automated multiwavelength Raman polarization and water-vapor lidar Polly^{XT}: the neXT generation

Ronny Engelmann[1], Thomas Kanitz[1], Holger Baars[1], Birgit Heese[1], Dietrich Althausen[1], Annett Skupin[1], Ulla Wandinger[1], Mika Komppula[2], Iwona S. Stachlewska[3], Vassilis Amiridis[4], Eleni Marinou[4,5], Ina Mattis[6], Holger Linné[7], and Albert Ansmann[1]

[1]Leibniz Institute for Tropospheric Research (TROPOS), Leipzig, Germany
[2]Finnish Meteorological Institute, Kuopio, Finland
[3]University of Warsaw, Faculty of Physics, Institute of Geophysics, Warsaw, Poland
[4]National Observatory of Athens, Institute for Astronomy, Astrophysics, Space Application and Remote Sensing, Athens, Greece
[5]Aristotle University of Thessaloniki, Department of Physics, Laboratory of Atmospheric Physics, Thessaloniki, Greece
[6]Deutscher Wetterdienst, Hohenpeißenberg Meteorological Observatory, Hohenpeißenberg, Germany
[7]Max Planck Institute for Meteorology, Hamburg, Germany

Correspondence to: Ronny Engelmann (ronny@tropos.de)

Received: 24 June 2015 – Published in Atmos. Meas. Tech. Discuss.: 24 July 2015
Revised: 26 February 2016 – Accepted: 18 March 2016 – Published: 25 April 2016

Abstract. The atmospheric science community demands autonomous and quality-assured vertically resolved measurements of aerosol and cloud properties. For this purpose, a portable lidar called Polly was developed at TROPOS in 2003. The lidar system was continuously improved with gained experience from the EARLINET community, involvement in worldwide field campaigns, and international institute collaborations within the last 10 years. Here we present recent changes of the setup of the portable multiwavelength Raman and polarization lidar Polly^{XT} and discuss the improved capabilities of the system by means of a case study. The latest system developments include an additional near-range receiver unit for Raman measurements of the backscatter and extinction coefficient down to 120 m above ground, a water-vapor channel, and channels for simultaneous measurements of the particle linear depolarization ratio at 355 and 532 nm. Quality improvements were achieved by systematically following the EARLINET guidelines and the international PollyNET quality assurance developments. A modified ship radar ensures measurements in agreement with air-traffic safety regulations and allows for 24/7 monitoring of the atmospheric state with Polly^{XT}.

1 Introduction

Lidar profiling of atmospheric aerosol and cloud layers has become important for climate research during recent decades. More recently, the volcanic eruption hazards of Eyjafjallajökull and Grimsvötn (Ansmann et al., 2010; Tesche et al., 2012) for aircraft safety have shown the need for a height-resolved monitoring of the aerosol concentration on continental scales. There are a few examples of how this can be achieved either by spaceborne applications, e.g., with the Cloud-Aerosol Lidar and Infrared Pathfinder Satellite Observations mission (CALIPSO, Winker et al., 2009) or by networks of ground-based aerosol profilers as organized in the European Aerosol Research Lidar Network (EARLINET, Bösenberg and Hoff, 2008; Pappalardo et al., 2014) and by the ceilometer network of the German Meteorological Service (DWD, Flentje et al., 2010). The disadvantage of the polar-orbiting lidar aboard CALIPSO is the low temporal resolution, because it overpasses the same area only every 16th day. Ceilometer networks are operated 24/7, but are not able to distinguish aerosol particles in terms of their mean size, shape, or extinction efficiency. Within EARLINET, now part of the Aerosols, Clouds, and Trace gases Research In-

fraStructure (ACTRIS[1] and ACTRIS-2[2]), aerosol and cloud profiling and characterization is performed with different Raman and polarization lidars three times per week. EARLINET members have developed lidar techniques and algorithms in order to harmonize the lidar measurements in Europe, to set up quality standards, to perform systematic test routines, and to improve data evaluation (e.g., Freudenthaler, 2008; Freudenthaler et al., 2010; Pappalardo et al., 2014; Belegante et al., 2016). However, most of those lidar systems are prototypes leading to a huge variety of partly manually controlled system setups.

For more than 10 years, at TROPOS the aim has been to develop sophisticated, portable lidar systems (Polly) with the capabilities of advanced EARLINET lidars and EARLINET quality standards, but dedicated to stand-alone operation at remote places. In previous years, these systems were successfully used within EARLINET and showed also promising applicability for 24/7 operation at supersites combined with cloud-radar measurements, e.g., the Leipzig Aerosol and Cloud Remote Observations System (LACROS, Wandinger et al., 2012). An important advantage of the Polly systems is the uniform data structure and therefore the easy-to-adjust software updates. All Polly lidars are operated within a network called PollyNET (Althausen et al., 2013; Baars et al., 2016; PollyNET, 2016) which ensures data backup, instrument monitoring, and an international transfer of knowledge.

The very first Polly (first generation), a single-wavelength Raman lidar, was developed in 2003 (Althausen et al., 2009). Since then, further lidar systems along the line of Polly have been developed and permanently upgraded. Since 2006, two multiwavelength Raman and polarization lidar systems with eXTended capabilities (Polly^{XT}, second generation) have been developed and operated by TROPOS and FMI. These systems enabled the determination of the particle backscatter coefficients at 355, 532, and 1064 nm and extinction coefficients at 355 and 532 nm (therefore often called $3+2$ lidars). The spectral backscatter and extinction coefficients allow for aerosol classification by optical properties of aerosol particles (Müller et al., 2007) and applying inversion algorithms (Müller et al., 1999; Baars et al., 2012) to derive the particle size distribution and concentration. In addition, a polarization-sensitive channel ($+1$) was installed to determine the shape of the aerosol particles from measurements of the (particle) linear depolarization ratio (Kanitz et al., 2013), to separate dust and non-dust particles in mixed aerosol layers (Baars et al., 2011), and to investigate mixed-phase clouds (Kanitz et al., 2011). In the framework of worldwide field campaigns these $3+2+1$ Polly^{XT} systems achieved a unique lidar data set in the Amazonian basin, India, China, South Africa, Finland, Chile, and over the Atlantic aboard the research vessels *Polarstern* and *Meteor*. Figure 1 shows impressions from a selection of the very different measurement locations.

Figure 1. Autonomous measurements of Polly^{XT} in **(a)** the Amazon basin, 2° S, at > 90 % relative humidity, **(b)** at Kuopio, Finland, 62° N, in winter, **(c)** aboard the RV *Polarstern* during 8 m ground swell, and **(d)** at the southern edge of Latin America, Punta Arenas, Chile, 52° S.

In 2009 and 2010, two additional Polly^{XT} lidars were developed with the setup described in Althausen et al. (2009). One has been operated stationary as a new EARLINET station (Preißler et al., 2013) at the Geophysics Centre of Évora (CGE, University of Évora, Portugal, now Institute for Earth Sciences, UE-ICT). The other one has been mounted at the meteorological monitoring station on Baengnyeong Island, Korea and has been operated by the Korean National Institute for Environmental Research (NIER).

In 2011, the Polly^{XT} systems of TROPOS and FMI underwent overall maintenance, upgrades of the optical setup, and were equipped with an additional water-vapor Raman channel (407 nm). The third generation of the systems was started in 2013, when another two systems with two depolarization channels at 532 and 355 nm were set up in cooperation with the University of Warsaw (UW) and in the framework of the mobile sea facility OCEANET-Atmosphere (Kanitz et al., 2013). The latter includes a second receiver unit for the near range at 532 and 607 nm with a full overlap in 120 m height above ground (Sect. 5.3) and an improved data acquisition unit (Sect. 2.3). In 2015, a similar near-range receiver with four channels (355, 387, 532, and 607 nm) was developed for the Polly^{XT}_UW system. Recently, two more systems following the UW and OCEANET design were finished and put into service at the National Observatory of Athens (NOA, Greece) and the Deutscher Wetterdienst (DWD, Hohenpeißenberg, Germany). Table 1 gives an overview of the Polly^{XT} family and the capabilities of the various systems.

[1] http://www.actris.net
[2] http://actris2.nilu.no

Table 1. Measurement capabilities of the different Polly systems at UV (355 nm), VIS (532 nm), and IR (1064 nm) wavelengths. Water-vapor (W/V) channels and absolute calibration of the depolarization channels (δ-cal.) have been installed in most of the systems. The four most recent systems include a near-range (N/R) telescope in addition at 532 and 607 nm wavelengths. A new setup with additional N/R channels at 355 and 387 nm wavelengths has been recently developed. Three different data acquisition (DAQ) systems have been in use so far (see Sect. 2.3).

System	Generation	Data since	UV	VIS	IR	W/V	δ-cal.	N/R VIS	N/R UV	DAQ
Polly 1st	1	Dec 2002	α, β							P7882
IFT*	2	Oct 2006	α, β	α, β, δ	β	×	×			P7882
TROPOSv	2	Jan 2015	α, β, δ	α, β, δ	β	×	×			CNT80
FMI	2	May 2007	α, β	α, β, δ	β	×	×			P7882
UE-ICT	2	Feb 2009	α, β	α, β, δ	β					P7882
NIER	2	Jan 2010		α, β, δ						P7882
OCEANET	3	Oct 2012	α, β, δ	α, β, δ	β	×	×	×	from Aug 2015	CNT80
UW	3	Jun 2013	α, β, δ	α, β, δ	β	×	×	×	from Apr 2016	CNT80
NOA	3	Sep 2014	α, β, δ	α, β, δ	β	×	×	×		CNT80
DWD	3	Apr 2015	α, β	α, β, δ	β		×	×		CNT80

* The system labeled IFT (former abbreviation of the Institute for Tropospheric Research) was upgraded with an additional UV depolarization channel and the new data acquisition in January 2015 and is now labeled TROPOS.

Since the system's presentation in 2009 (Althausen et al., 2009) the numerous improvements of Polly^{XT} build up a neXT generation of Polly^{XT}s that are the topic of the present paper. At the beginning of the paper, we give an overview about the first developed third-generation system Polly^{XT}_OCEANET. Afterwards, we show recent improvements of Polly^{XT} in terms of an additional detection channel for water-vapor profiling (Sect. 3), adjustments in the optical setup to determine the particle linear depolarization ratio (Sect. 4), and achievements in the critical overlap range for lidar systems (Sect. 5). Finally, we present a case study of observed marine and dust layers from measurements aboard the research vessel *Meteor* to show the capabilities of the new generation of our sophisticated Pollys. A conclusion and outlook section is given at the end.

2 Systems

This section gives an overview of the general concept of the Polly^{XT} lidars. The optical setup and the new photon-counting data-acquisition system are described. The quality-assurance procedures which we apply are presented at the end.

2.1 Overview

Figure 2 presents the simple concept of our lidar. The Polly systems are housed in an outdoor cabinet, or in the case of Polly^{XT}_OCEANET, in a container to allow the operation under various climatic conditions. The systems run autonomously by programmed measurement procedures and can be fully controlled by remote access via the Internet. In case of rain events, measurements are automatically interrupted and resumed thereafter. When required by air-safety regulations, the system can be attached to a modified FURUNO radar (Duck et al., 2005) in order to shut off the laser beam in case an airplane is detected in a $\pm 15^\circ$ cone above the lidar.

In terms of maintenance, the systems require much less attendance than many manually operated research Raman lidars used in EARLINET. The Pollys only need cleaning of the exit windows (if necessary), laser maintenance (flash lamp replacement) every 3 months, occasional realignment of the laser beam, and exchange of neutral-density filters (if aerosol conditions change significantly). In extreme climatic conditions, the internal heating has to be adapted. Since Polly^{XT}_OCEANET (generation 3) we apply a laser system which requires an external coolant-water supply whereas before (generation 2) the laser systems were cooled by air. By using the external-coolant water, the cabinet temperature can be kept more constant and also the laser system operates more reliable and independent of external climatic conditions.

Within PollyNET, a development of an internal automatic data analysis was needed. At the web page of PollyNET, automatically retrieved profiles of the backscatter and extinction coefficient are presented each 30 min, whenever atmospheric conditions are favorable for an automated retrieval (Baars et al., 2016). These developments have been made in parallel but also in consistency with the automatic software developments within the framework of EARLINET and ACTRIS. Promising results were achieved during previous tests (D'Amico et al., 2015, 2016; Mattis et al., 2016). For EARLINET the single calculus chain (SCC) has been developed to automate and harmonize the lidar data analysis within the network, while within PollyNET the data analysis benefits from the equal hardware and data format standards. The methodology and the results from the last 10 years of

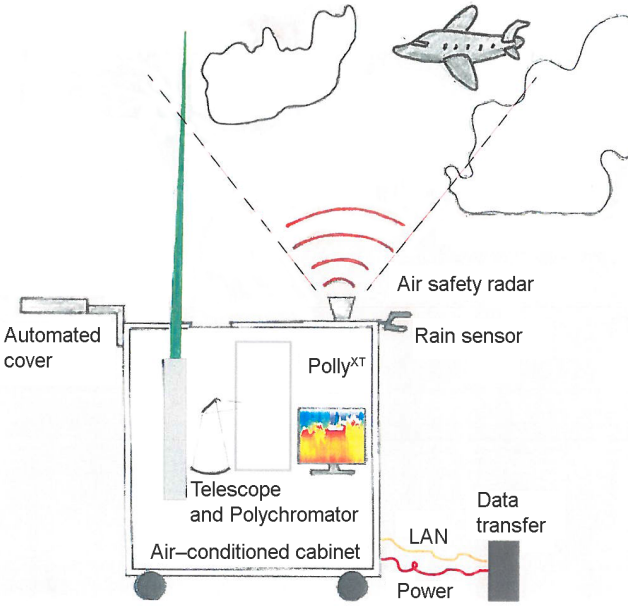

Figure 2. The general concept of Polly. These unattended aerosol Raman lidars have already been deployed worldwide for campaigns with periods on the order of 1 year. They are completely controlled via remote access, automatically shut down in events of rain, can be connected to an air-safety radar, and transfer the data to a centralized data server where the data are archived and automatically evaluated. Issues with data quality can thus be quickly identified and the users are informed. The system's mass is approximately 500 kg, but they can be easily moved on the four wheels.

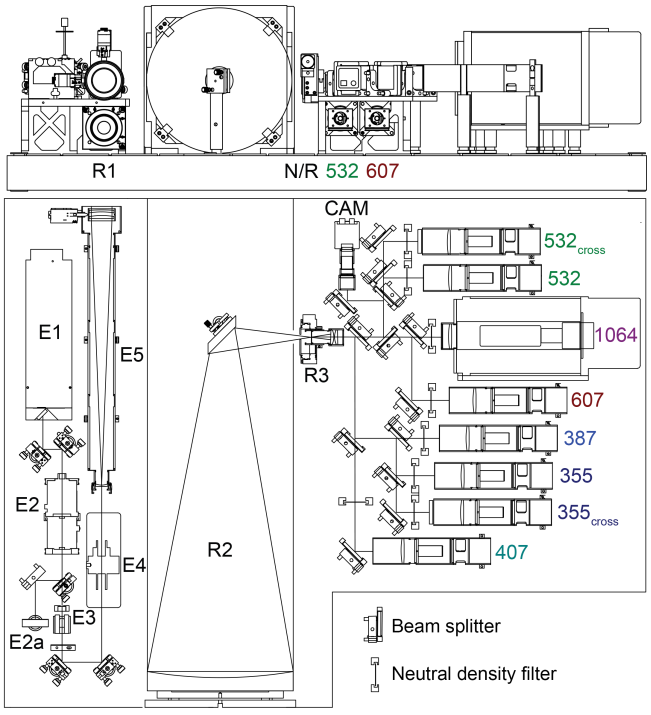

Figure 3. The optical setup of Polly^{XT}_OCEANET. The upper part displays a top view and the lower part the front view of the system. Details are explained in the text.

measurements within PollyNET are presented in Baars et al. (2016).

2.2 Optical concept

Because it is the most complex Polly system so far, the optical setup of Polly^{XT}_OCEANET is presented in Fig. 3. In Polly^{XT}, the operated laser is an Inlite III-20 from Continuum (Althausen et al., 2009). The laser emits light pulses at 1064 nm with a repetition frequency of 20 Hz. The position of the laser head in the optical setup is denoted by E1 in Fig. 3. The alignment of the laser beam through the external second and third harmonic generators (SHG, THG, type II, originally from Continuum Surelite laser, E2 in Fig. 3) was improved by using a more rigid setup as well as by predefined adjustment apertures compared to the original setup. With this upgrade it is easier to correctly realign the beam after a maintenance procedure or after an exchange of the entire laser. SHG and THG are heated to approximately 70 °C by two independent temperature controllers which can be adjusted in order to remotely optimize the conversion efficiencies. After SHG and THG laser pulses with energies of 180 mJ at 1064 nm, 110 mJ at 532 nm, and 60 mJ at 355 nm are emitted. The laser power is logged by means of a laser-internal sensor during the measurements, and an external power meter (E2a) is used to measure solely the UV component in order to observe the conversion efficiency continuously for later quality control.

The purity of the linear polarization of the pulses at all wavelengths is subsequently ensured by the use of a waveplate and a Brewster-cut Glan–laser polarizer (E3 in Fig. 3). Further explanation is given in Sect. 4.1. The light is redirected upwards via two dichroic mirrors. An additional shutter is denoted E4 in Fig. 3. The shutter is controlled from a modified FURUNO ship radar and prohibits the emission of laser light during airplane overflights. Finally, the 7 mm beam of the Inlite III is expanded to 45 mm diameter with a beam expander (E5 in Fig. 3) before the light is emitted into the atmosphere.

The far-range receiver unit of all Polly^{XT} systems includes a Newtonian telescope (R2 in Fig. 3) with a 300 mm primary mirror. A device for the absolute calibration of the depolarization measurements is mounted in front of the pinhole (R3, see Sect. 4.3). The pinhole itself has a diameter of 0.9 mm. Thereafter, a lens pair collimates the received light. Dichroic beam splitters separate the radiation by wavelength. The stability of the laser-beam overlap with the receiving telescope is monitored with a camera (CAM) that is synchronized to the laser trigger and observes the transmitted beam at 532 nm. It can be estimated that a laser-beam alignment error of ±0.1 mrad can be detected by this approach. The pictures of the overlap are used for real-time monitoring and are

stored for long-term system performance analysis. The camera and all receiver channels are equipped with interference filters for background suppression (see Table 2 for detailed information). Planoconvex lenses in front of each photo multiplier tube (PMT) are used to project an image of the primary mirror onto the photo cathode in order to minimize influences of inhomogeneities of the sensitivity of the photo cathodes which can otherwise result in range-dependent deviations of the lidar signal (Simeonov et al., 1999; Freudenthaler, 2004).

Photon counting is performed for all channels. Small PMT modules from Hamamatsu (type: H10721P-110) are used for all wavelengths, except for the 1064 nm wavelength. Here, a Hamamatsu R3236 is applied which is cooled below −30 °C with a multi-stage thermo-electric cooler (see Fig. 3).

Polly^{XT}_OCEANET includes an additional near-range receiver unit (R1, see Sect. 5.3) to lower the overlap-affected height range of the overall system to 120 m above the lidar, i. e., to decrease the minimal measurement height in the planetary boundary layer. In this way, better closure measurements in combination with in situ measurements can be performed. Table 2 summarizes the general parameters of the original Polly^{XT}_OCEANET configuration. It should be noted that the system recently has been upgraded with a four-wavelength near-range receiver (355, 387, 532, 607 nm wavelengths) that was originally developed together with the University of Warsaw.

The optical setup of Polly^{XT}_OCEANET was mounted on a weight-saving carbon-fiber optical board (Carbon Vision), which saves approx. 120 kg of weight compared to the original version of Polly^{XT}. The entire board is tilted by 5° to avoid specular reflections from horizontally aligned ice crystals which otherwise can prohibit the correct determination of the cloud phase by depolarization measurements (e.g., Seifert et al., 2010).

In contrast to the former systems of generation 1 and 2, which were described by Althausen et al. (2009), we took a new approach and designed the recent systems with a 3D-CAD software that allows for much faster and more consistent manufacturing of future systems. Also analysis by the finite-element method (FEM) can be performed in order to determine the deformation of optical mounts under temperature or gravitational stresses. Since the optical elements are aligned on a carbon-fiber optical board and alignment is performed horizontally, possible misalignments during the vertical mounting of the board in the cabinet can be minimized. For example, the deformation of the optical mount of the primary mirror during the vertical installation is depicted in Fig. 4. The shift of the field of view resulting from this tilt of the primary mirror can be estimated to be on the order of only 0.02 mrad from this figure which is within an acceptable margin.

Table 2. Specification of the portable Raman lidar Polly^{XT} (generation 3). N/R denotes the near-range receiver unit.

Size	1.8 m × 1.7 m × 0.8 m
Weight	500 kg, movable by 4 wheels
Power	≈ 2 × 1.5 kW (lidar and air condition)
Transmitter	
Laser	Inlite III-20 (Continuum)
SHG and THG	external, type II, from Surelite series
Repetition rate	20 Hz
Energy after THG	180 mJ (1064 nm), 110 mJ (532 nm), 60 mJ (355 nm)
Beam diameter	7 mm
Beam divergence	< 1.5 mrad (full angle, 86 % of energy)
Pointing stability	< 0.5 mrad (estimated)
Polarization	s-pol (with respect to the beamsplitters), cleaned by Glan–laser polarizer
Beam expander	6.5×, achromatic
Beam divergence	< 0.2 mrad (full angle, 86 % of energy)
Beam alignment	by means of a triggered camera
Receiver	
Far range	
Type	Newtonian
Diameter	300 mm (primary mirror) 76 mm (secondary flat mirror)
Focal length	900 m
Position of secondary	700 mm from primary
Material	Pyrex
Laser axis distance	240 mm (laser – primary)
Field of view	1 mrad (full width, 0.9 mm diaphragm)
Collimator lens pair	Thorlabs LA1907 and LA1031
Focusing lens	Thorlabs LA1401 Thorlabs LA1050 (only at 1064 nm)
Near range	
Type	refractor (Thorlabs AC508-250-A)
Diameter	50 mm
Focal length	250 mm
Laser axis distance	98 mm (laser – lens)
Field of view	2.2 mrad (full width)
Receiver fiber	550 µm, Thorlabs M37L02
Fiber scrambler	2 mm sapphire ball lens
Collimator lens	Thorlabs AC127-019-A
Detection:	
Channels [nm]/ bandwidth [nm]	1064/1.0, 607/0.3, 607 (N/R)/0.3, 532/1.0, 532 (cross)/1.0 , 532 (N/R)/1.0 407/1.0, 387/0.3, 355/1.0, 355 (cross)/1.0
Photomultiplier	Hamamatsu H10721P-110 Hamamatsu R3236 (only at 1064 nm)
Signal acquisition	600 MHz photon counters, 7.5 m height resolution, up to 48 km, pretrigger

2.3 Data acquisition

The data acquisition of the Polly^{XT} systems of generation 1 and 2 had several drawbacks. For example, only a maxi-

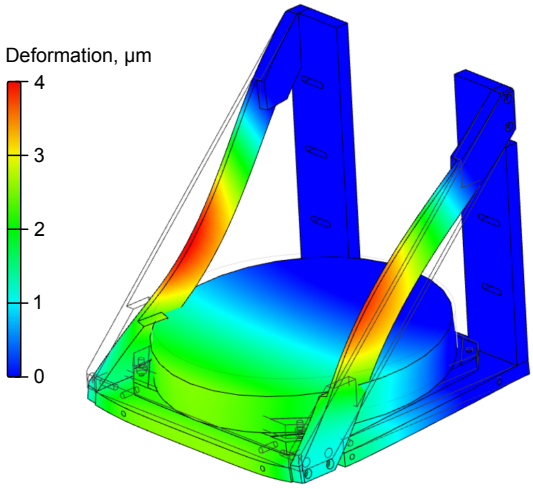

Figure 4. FEM calculations of the maximal deformation of the mount of the primary mirror during the vertical adjustment in the cabinet. The deformation intensity is given by the color code.

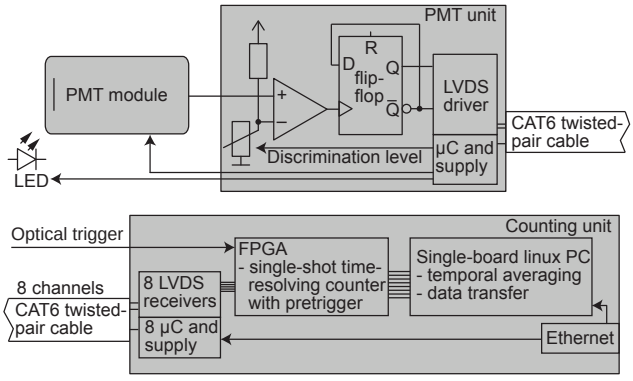

Figure 5. Scheme of the eight-channel photon-counting system (CNT80). Each PMT and the discrimination electronics are constructed as a fixed unit (top panel). The photon pulses from a maximum of eight detector units are then digitally transferred to the counting unit (bottom panel) where the lidar return signals are processed, averaged, and can be obtained by the measurement PC via an Ethernet connection.

mum of 8 channels (four P7882 PCI cards, FAST ComTec, GmbH) could be handled by one measurement PC. External preamplifiers had to be used and the 2 m long signal cables had to run from the detectors to the PC which might have caused electromagnetic induced distortions from the laser nearby. Hence, a new photon-counting data acquisition hardware which was developed at the Max Plank Institute for Meteorology in Hamburg has been applied to all recent Polly^{XT} systems (generation 3). The aim of the project CNT80 was to develop a small and low-cost data acquisition for lidar measurements with a signal dynamic range that is only determined by the detectors themselves. Minimum single-photon pulse lengths of are on the order of 2 ns for our employed PMTs. Thus the maximum count rates that need to be handled by the electronic design are above 500 MHz in order not to increase the overall dead-time effects significantly.

Figure 5 shows the general electronic concept of the counting unit. For all channels except the 1064 nm channel we apply Hamamatsu modules H10721P-110. Within a few centimeters behind these modules the pulse discrimination is performed, so that electronic interference is kept to a minimum and the pulses are digitized as early as possible. In order to increase the maximum electronic count rate and reduce possible additional dead-time effects, the digital signals are immediately fed into a flip-flop circuit which alters its logic output level every time a photon was detected. This way, each voltage-level transition after the flip flop between the differential outputs Q and $\bar{Q}$ corresponds to one photon event and the transfer frequency towards the time-resolving counter is divided in half. Then, an LVDS (low-voltage differential signaling) driver is used to match the impedance of a standard CAT6 Ethernet cable for data transfer. Additionally, a micro controller (µC) is implemented to adjust the pulse-discrimination level and the PMT voltage, to switch the power supply, as well as to control an LED (light-emitting diode) which can be used for various test procedures of the PMT. For example, the relative sensitivity of a PMT can be tracked over its lifetime by this LED. Also the dead time could be derived as shown in Johnson et al. (1966) by observing the deviation of the single-photon counting distribution from an ideal Poisson distribution at high count rates.

A single counting unit (Fig. 5, bottom) is capable to control and to acquire the data of eight detection channels and, if required, several of these units can be easily used in parallel. An optical trigger taken from laser stray light starts the time-resolving counter which is implemented in an FPGA (field-programmable gate array) board (Virtex-4 FX12 Mini-Module). Each single-shot lidar profile is then transferred from the FPGA to an embedded Linux PC (ADSP-BF537 STAMP) where the profiles are averaged over a predefined time period of typically 30 s. Via an Ethernet connection the averaged lidar profiles can then be obtained by a measurement PC. Also the controlling of the PMT units (power, setting of high-voltage and discrimination level, external LED control) takes place over Ethernet. The specifications of the new data acquisition are summarized in Table 3.

When using photon counting, dead-time effects need to be considered if the data acquisition operates in high count-rate regimes (Donovan et al., 1993; Whiteman et al., 2003), i.e., at signals above 10 million counts per second (10 Mcps) for our system. In the classical sense, the counters have to be considered *paralyzable* as too many photons per time interval will pile up and will finally result in a lack of voltage-level crossings at the discrimination level. Thus ambiguity can occur at very high signals (> 100 Mcps).

We performed measurements with each PMT in a laboratory setup in order to measure their dead-time effects prior to their installation. We applied an LED which delivers a tri-

Table 3. Specification of the new CNT80 data acquisition hardware as applied in Polly^{XT}.

Number of channels	8
Height resolution	7.5 m
Maximum altitude	≈ 40 km
Pre-trigger	≈ 256 bins
Electronic count rate	> 600 MHz (sine-wave)
Discriminator level	−5.8 mV (typical)
PMT voltage	H10721P-110: 1.15 V (control voltage)
	R3236: −2000 V
Max. PMT count rate	60 Mcps (80 Mcps dead-time corrected)
Overall dead time	2–4 ns (varies with individual PMT)
Dark counts	< 50 cps, < 1500 cps (R3236)
Trigger	optical fiber from laser stray light
Maximum laser pulse repetition rate	80 Hz
Connection	PMT control/data readout via Ethernet

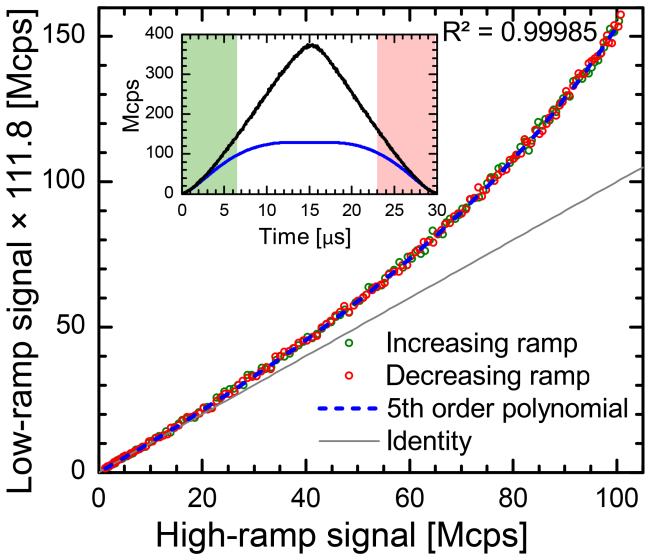

Figure 6. Measurement of dead-time effect of the 355 nm PMT of Polly^{XT}_TROPOS: a light ramp was detected with high and low (by use of an attenuator) count rates, respectively. The inset shows the light ramps with high count rates (blue) and with low count rates (black) but scaled (by a factor of 111.8) so that both curves match the identity line at count rates < 10 Mcps. The main graph shows the dead-time correction function which results from plotting the true count rate (black line from the inset) over the measured count rate (blue line). In addition, a 5th-order polynomial fit which can be applied for dead-time correction is shown.

angular pulse onto the PMT and measure the pulse shape with low count rates (< 5 Mcps) by applying neutral-density filters. In this way we measured the pulse shape undisturbed from dead-time effects. Afterwards, we performed the same measurement with higher maximum count rates (> 100 Mcps). Figure 6 shows the result of such a measurement. The inset graph shows the two signals from the light ramps. The blue curve was obtained with a high light level and is therefore flattened at the maximum. The black line was calculated from the measurement with less light but is scaled to linearly match the blue curve at low count rates from 0–10 Mcps.

The main graph shows the correlation between the two lines from the inset separated for the increasing (green) and decreasing (red) paths of the light ramp, respectively. Both paths are identical and show that no issues with after-pulsing or signal-induced noise effects are apparent. This data also showed that the paralyzable theory is not always adequate for count rates higher than 40 Mcps and differences to the model occur. In fact, for some PMTs the *non-paralyzable* model seemed to fit better to the dead-time-affected slope. Measurements from 32 different PMT-modules showed that the typical dead times with respect to the paralyzable and non-paralyzable theory are 3.2 ± 0.6 and 3.4 ± 0.5 ns, respectively, in the range of 0 to 60 Mcps. Up to now only one 1064 nm PMT was measured (Polly^{XT}_DWD) and a dead time of 2.8 and 3.3 ns, respectively, was derived according to both theories.

In addition, the correction according to the paralyzable theory requires an iterative and thus time-consuming calculation. Therefore, the data points shown in Fig. 6 were fitted by a 5th-order polynomial and the coefficients and their errors are stored in the raw-data files for each channel separately. The derived polynomial coefficients which can be used for correction of the lidar-signal count rate (in Mcps) are from 0 to 5th order $0, 0.973, 3.5 \times 10^{-3}, -7.9 \times 10^{-6}, 1.1 \times 10^{-7}$, and 1.4×10^{-9}, respectively, for the shown channel. This way, correcting of the dead-time effects in the post-processing line can be performed automatically. Although Fig. 6 shows that a dead-time correction of a measured signal of 100 Mcps might be possible, we try to keep the measured signals below 60 Mcps in order to keep the correction reasonable (max. correction factor of 1.3). Further studies might be needed to explore the full benefits from the dead-time correction scheme in terms of increasing the signal dynamic range.

2.4 Quality assurance procedures

Within EARLINET several quality-assuring guidelines and algorithms have been developed in order to harmonize the lidar measurements, to set up quality standards, to perform systematic test routines, and to improve the lidar data evaluation (e.g., Böckmann et al., 2004; Pappalardo et al., 2004; Freudenthaler, 2009a; Pappalardo et al., 2014; Wandinger et al., 2016). In order to check the alignment of a new system and to identify potential systematic signal errors, we perform comparative measurements with other independent lidar systems at TROPOS. This way discrepancies of the retrieved data products could be noticed early. Further quality assurance schemes that are applied for Polly^{XT} data and that are more related to data evaluation routines such as cloud

screening, Rayleigh fit, and signal-to-noise analysis are given in Baars et al. (2016).

Additionally, the telecover test (Freudenthaler, 2008) is performed regularly and especially after transportation of the systems. Measurements from different quarters of the primary mirror are performed by vignetting the remaining three quarters. Some selected results from such a telecover test with the Polly^{XT}_NOA system is shown in Fig. 7. The open quadrants for each of the consecutive measurements are labeled north, east, south, and west. The measurement of the north sector was repeated at the end of the measurement cycle (N2) in order to detect atmospheric changes during the test. The top graph shows the fraction of each sector to the total lidar signal at 387 nm [e.g., N/(N + E + S + W), black line]. As expected, the north sector of the telescope (closest to the laser beam) detects most of the signal below 500 m height. The signals from the east and west sectors are similar although the east sector is vignetted by the mount of the secondary mirror and therefore accounts for less than 25 % of the signal above 700 m height. The signal of the south sector reaches the 25 % fraction as the last one. From this graph it can be seen that the height of the full overlap of the 387 nm channel is between 700 and 800 m height (also see Fig. 11) as the quadrant fractions remain constant above that height.

The center graph of Fig. 7 shows the signal ratio of the 532 and 607 nm channels as it is used for the Raman method of the calculation of the backscatter coefficient (Ansmann et al., 1992) for each quadrant separately. The curves are normalized between 1.5 and 2.0 km height, at a range where the overlap function is unity. It can be seen that the signal-ratio differences between the sectors are smaller than the atmospheric variability (N and N2 sector) down to 250 m. Hence we can assume that the relative error of the signal ratio which might arise from different overlap functions of the two channels is below 10 % for heights greater than 250 m. A similar argument holds for the channels used for the calculation of the 532 nm volume linear depolarization ratio shown at the bottom graph of Fig. 7. The ratios of the 532 nm cross-polarized and total signals are within a margin of 10 % down to 300 m height for all sectors for this system. Again, the atmospheric variability caused a larger difference during this measurement as seen from the difference of the N and N2 ratios.

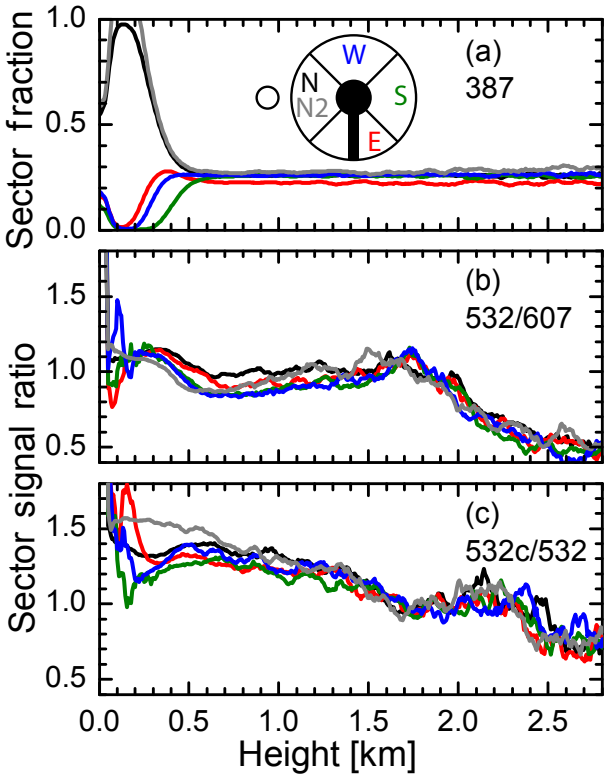

Figure 7. Telecover test measurement of Polly^{XT}_NOA on 25 May 2015. Measurements of 15 min duration were taken for each of the telescope sectors (north, east, south, and west with respect to the laser beam) as indicated in **(a)**. The signals were smoothed for 75 m range. The measurement of the north sector was performed twice (N2) with a time difference of 1 h in order to account for atmospheric variability. **(a)** signal fraction of each sector to the sum of all sectors (N + E + S + W). **(b)** signal ratios of the 532 and 607 nm wavelength channels for each sector. The curves were normalized to 1 between 1.5 and 2 km. **(c)** same as **(b)** but for the cross-polarized and total channels at 532 nm wavelength.

3 Water-vapor measurements

Operational aerosol lidar systems can be even more valuable if they have the simultaneous capability to monitor the atmospheric water vapor. Water vapor is the most important greenhouse gas in the Earth's radiation budget and controls aerosol optical properties. Vertical profiles of the water-vapor mixing ratio can serve as input value for height-resolved radiative-transfer calculations and to investigate the hygroscopicity of aerosols and the processes of cloud formation. For some systems (see Table 1) the setup includes an additional channel at 407 nm for the detection of Raman-scattered light from water vapor (e.g., Wandinger, 2005). An automated calibration scheme by use of a microwave radiometer was recently presented in Foth et al. (2015).

Figure 8 shows one of the first measurements of the water-vapor mixing ratio with Polly^{XT}_IFT. The measurement took place at Leipzig on 10 February 2012 from 19:00 to 20:30 UTC. The comparison with a co-located radiosonde launch and with the EARLINET Raman lidar MARTHA (Multiwavelength Aerosol Raman Lidar for Temperature, Humidity, and Aerosol profiling, 80 cm telescope, 350 mJ at 355 nm, 30 Hz, Mattis et al., 2002) shows very good agreement, even under these relatively dry conditions with less than 1.5 g kg^{-1} of water vapor in the planetary boundary layer. The difference between the two lidar measurements is less than 0.2 g kg^{-1} up to 5 km height. Some-

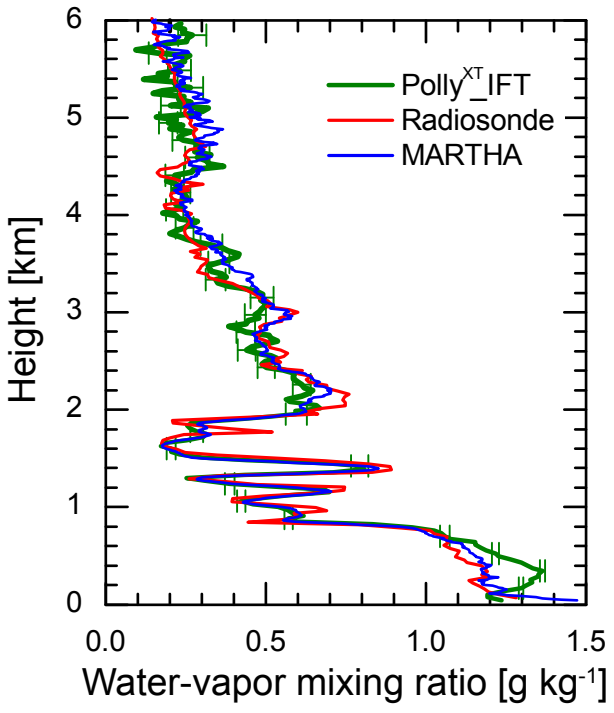

Figure 8. 90 min mean profiles of the water-vapor mixing ratio as determined with Polly^{XT}_IFT (green, 30 m vertical smoothing up to 2 km height, 60 m above), a co-located radiosonde (red), and coincident measurements of the EARLINET Raman lidar MARTHA (blue, resolution 30 m) at Leipzig on 10 February 2012 (19:00–20:30 UTC). The error bars are calculated from the signal noise.

what larger differences between lidar and radiosonde data might be caused by the drift-off of the radiosonde. A measurement close to the ground (> 200 m height) is feasible because the water-vapor mixing ratio calculates from the 407 to 387 nm signal ratio and if the overlap functions of both channels are equal they cancel each other out (e.g., Wandinger, 2005). The reason for the deviations on the order of 0.2 g kg^{-1} (16 % error) of the Polly^{XT}_IFT data below 800 m height from MARTHA and the radiosonde data remains unclear for the presented measurement. Either electronic distortions by the older P7882 data acquisition setup or different overlap functions for 387 and 407 nm might have caused the discrepancy.

The presented data were obtained from a night-time measurement. The low Raman-scattering cross section of water vapor does not allow measurements during daytime with the current Polly^{XT} setup. Moreover, the water-vapor detector is automatically switched off during daytime, because the daylight background intensity can be near the damage threshold of the PMT.

4 Determination of particle linear depolarization ratio

The linear depolarization ratio has gained importance for aerosol and cloud layer separation (Liu et al., 2010), as well as cloud and aerosol type identification (Sassen, 2005; Omar et al., 2009). In addition, the particle linear depolarization ratio is well suited to characterize aerosol particles (Freudenthaler et al., 2009b; Preißler et al., 2013) and to separate dust and non-dust particles mixed aerosol layers (Tesche et al., 2009; Ansmann et al., 2011; Baars et al., 2012; Kanitz et al., 2013). Even fine and coarse-mode dust can be separated by means of polarization lidar and Sun photometer measurements (Mamouri and Ansmann, 2014). These approaches require measurements of depolarized light with high accuracy.

Moreover, measurements of the particle linear depolarization ratio at two different wavelengths simultaneously can help to study aerosol mixtures and separate their components. The spectral slope of the aerosol depolarization is sensitive to the ratio of the fine and coarse mode of non-spherical particles (Sakai, 2010; Burton et al., 2012).

4.1 Laser polarization

The linear depolarization ratio of Rayleigh scattering is smaller than 1.5 % in dependence of the width of the used interference filters (Behrendt and Nakamura, 2002). In case of Polly^{XT} (filter width of 1.0 nm) molecular linear depolarization ratios of 0.75 and 0.53 % are expected at 355 and 532 nm, respectively, assuming 100 % purity of the linearly polarized emitted laser light. The purity of linear polarization of typical flash-lamp-pumped and Q-switched Nd:YAG laser systems at the fundamental wavelength is about 98 to 99 %. Birefringence in the laser rod usually induces small amounts of cross-polarized light.

In contrast, the generation of second and third harmonic radiation can significantly decrease the purity of polarization or rotate the plane of polarization and thus affect the accuracy of measurements. SHG and THG are both of type II in the current Polly^{XT} setup, i.e., the radiation at 355, 532, and 1064 nm is vertically, horizontally, and elliptically polarized, respectively, with respect to the optical board. But because of the original mounting design of the Continuum Surelite SHG and THG the crystal planes are not perfectly aligned with respect to the optical board and the laser polarization planes could be rotated by a few degree. A common approach to purify the linear polarization of the laser light and to align the polarization plane is to separate the beams, polarize them, and afterwards recombine the beams onto one axis or even transmit the beams separately. In contrast, we implemented a multiwavelength polarizer setup without prior beam separation for a convenient beam alignment, for stability, and for combined beam expansion afterwards. Figure 9 shows the approach to generate highly polarized light from the three Nd:YAG wavelengths. A quartz-crystal wave plate with different retardations at the three fundamental wavelengths was

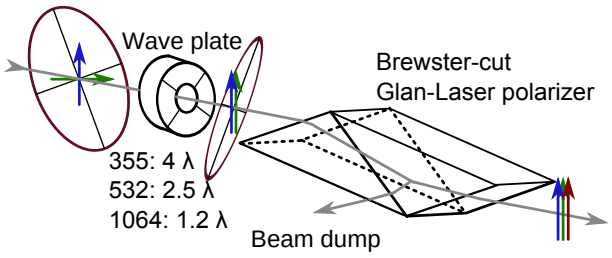

Figure 9. Wave plate and polarizer setup used to generate highly linear-polarized light at three wavelengths. The different polarization states after SHG and THG are matched by the wave plate and afterwards purified by the polarizer.

manufactured (Bernhard Halle Nachfl. GmbH, Berlin, Germany) in order to rotate the polarization plane at 532 nm (2.5 λ) but not at 355 nm (4 λ). At 1064 nm (1.2 λ) the light is elliptically polarized, and by inserting the wave plate either at +45 or −45°, the vertically polarized component can be maximized. After the wave plate, a Brewster-cut Glan–laser polarizer (Artifex Engineering, Emden, Germany) is inserted, which provides an extinction ratio of $< 5 \times 10^{-5}$ over a wavelength range from 350–2300 nm with an angular beam separation of < 0.01 mrad. Hence, the polarization impurity (fraction of non linear polarized light) of the transmitted laser beam is well below 0.1 % and thus sufficiently lower than the expected Rayleigh depolarization. The remaining offset angle between the laser polarization plane and the receiver beam-splitter plane can be reduced below 0.1°.

It was recently discovered that the beam expander (see Sect. 5.1) after the Glan–laser polarizer can introduce further effects. Unfortunately, stress-induced birefringence developed during the anti-reflection coating process of the calcium fluoride lenses (see Table 5). The resulting birefringence pattern might again introduce circular or unpolarized laser-light components which could explain the observed apparent linear volume depolarization ratio for Rayleigh scattering of > 1.5 % for the NOA and DWD systems. A replacement of the crystalline lens material by an amorphous glass type is foreseen.

4.2 Polarization effects of beam splitters

Dichroic beam splitters show different transmissions for parallel and cross-polarized (p and c-polarized) light which results in different transmission efficiencies for both polarization states at each detection channel. Mattis et al. (2009) showed systematic errors of lidar signals because of polarization-dependent receiver efficiencies in the presence of depolarizing aerosols, which can result in discrepancies of > 60 % in the total particle backscatter coefficient. In order to keep the error on the backscatter coefficient below 5 %, the receiver transmission ratios

$$R_i = \frac{\eta_{\mathrm{i,c}}}{\eta_{i,\mathrm{p}}} \quad (1)$$

of the total channels should be between 0.85 and 1.15. Here, $\eta_{\mathrm{i,c}}$ and $\eta_{i,\mathrm{p}}$ denote the detection efficiency of a channel i for cross and parallel-polarized light with respect to the laser polarization plane.

Overcoming this bias is possible, if the volume linear depolarization ratio (δ^{v}) at the respective wavelength as well as the receiver transmission ratios R_i are known for the channels. With these parameters the corrected lidar signals $P_{i,\mathrm{corr}}$ can be calculated from the measured signal P_i (Mattis et al., 2009):

$$P_{i,\mathrm{corr}} = P_i \frac{1 + R_i \delta^{\mathrm{v}}}{1 + \delta^{\mathrm{v}}}. \quad (2)$$

In principle, a good polychromator design should result in values of R_i of about 1 for the total elastic-backscatter channels so that the former correction is not necessary. In turn, high values of R_i (> 500) are desired for the polarization-sensitive channels. For Raman channels R_i is negligible since the molecular depolarization is nearly constant with height and changes only slightly with temperature in dependence of the width of the applied interference filter in these channels.

Although the remaining bias from non-ideal beam splitters can be corrected with Eq. (2), it yields another step in the data evaluation and can introduce new errors. Under this consideration, several beam splitters were substituted in the TROPOS and FMI Polly^{XT}s during the upgrade. The obtained values for the newest design of Polly^{XT} (DWD and NOA) are satisfactory and show a sensitivity ratio of each channel for parallel and cross-polarized light between 0.85 and 1.15 as suggested by Mattis et al. (2009). Table 4 gives an overview on the actual values of R_i and their measurement uncertainties. For the systems with R_i values outside this margin the correction with Eq. (2) should generally be considered.

A suitable method to determine R_i is to use an artificial light source with a polarizer mounted in front. By using this setup, the receiver efficiencies can be measured in dependence of the incident polarization plane and R_i can be obtained. We used a fiber-coupled halogen (visible and near-infrared radiation) and deuterium (ultraviolet radiation) lamp, a collimator lens, and a Glan–Taylor polarizer in a motorized rotation mount. The rotation mount with the polarizer was then mounted in front of the receiver telescope and the collimated light beam (diameter 15 mm) was aligned onto the field-stop aperture. Measurements of the received light intensity were performed for different polarization angles in steps of 1°. The polarization-dependent receiver efficiencies were then obtained from ratio of the signals for crossed (horizontal to the optical board) and parallel (vertical to the board) polarizations with respect to the laser polarization plane.

4.3 Calibration of the linear depolarization ratio

Depolarization measurements are performed with all Polly^{XT} systems (Table 1) at 532 nm and partly at 355 nm, too. In the past, the Rayleigh calibration method was applied within the

Table 4. Ratios of polarization-dependent receiver efficiencies R_i for the elastic channels of different Polly^{XT} systems.

Channel	TROPOS	FMI	OCEANET	UW	DWD	NOA
355_{total}	0.89 ± 0.08	1.25 ± 0.03	0.70 ± 0.02	0.8 ± 0.02	0.95 ± 0.03	1.00 ± 0.01
355_{cross}	> 1000	not installed	> 500	> 400	not installed	> 500
532_{total}	1.43 ± 0.01	1.02 ± 0.02	1.09 ± 0.04	1.02 ± 0.02	0.95 ± 0.02	0.89 ± 0.02
532_{cross}	> 700	> 700	> 800	> 800	> 1000	> 800
1064_{total}	1.03 ± 0.02	0.80 ± 0.03	1.08 ± 0.02	0.94 ± 0.04	1.13 ± 0.03	to be measured

data analysis under the assumption of pure Rayleigh depolarization in an aerosol-free height range (Behrendt and Nakamura, 2002). However, this method includes large uncertainties (e.g., Reichardt, 2003).

An alternative method is the $\Delta 90°$-calibration (formerly known as $\pm 45°$-calibration, Freudenthaler et al., 2009b; Freudenthaler, 2016). In order to include this method to the automatic measurement procedure of Polly, a remote-controlled rotary mount with a polarizer close to the focal plane of the receiver telescope was added to the system. This sheet polarizer (LPG23, ITOS GmbH, Mainz, Germany) is equipped with an off-center hole to measure without the polarizer into the light path in normal mode by rotating the hole onto the optical axis. Three times per day, the polarizer is rotated automatically under $+45$ and $-45°$ with respect to the laser polarization plane in the light path for calibration. Then, the volume linear depolarization ratio δ^{V} from the ratio $\delta' = P_c/P_t$ of the cross-polarized (c) and the total (t) signal is given by

$$\delta^{V} = \frac{1 - \delta'/C}{\delta' R_t/C - R_c}, \quad (3)$$

with the absolute calibration

$$C = \frac{1 + R_t}{1 + R_c}\sqrt{\delta'_{+45}\delta'_{-45}}, \quad (4)$$

following Freudenthaler et al. (2009b). The transmission ratios $R_{t,c}$ for total and cross-polarized radiation were determined as explained in Sect. 4.2. Figure 10 shows the time series of the determined calibration constant C during routine measurements of Polly^{XT}_IFT. The constant shows stable values with a variability caused by the signal noise. Changes of the neutral-density filters in front of the detectors have a significant effect on the calibration constant. For the period from 7 August to 19 October 2012, C was 0.090 ± 0.004, from 19 October to 14 November 2012 0.170 ± 0.008, and from 20 December 2012 to 7 March 2013 0.080 ± 0.01 %. The higher variability in the last period is based on short-time changes in the settings. At the end of November 2012 the fluctuations are caused by low signal-to-noise ratios.

For the error propagation of the volume linear depolarization ratio several aspects need to be taken into account. For example, the experimentally determined R_i values used in Eq. (3) have a measurement uncertainty which needs to be considered. The laser linear polarization purity, a possible angle between the laser polarization plane and the receiver optics, and the uncertainties involved in the measurement of the calibration constant (see Fig. 10) are further causes of uncertainty. Belegante et al. (2016) recently presented an extended analysis of different depolarization calibration procedures and their related uncertainties.

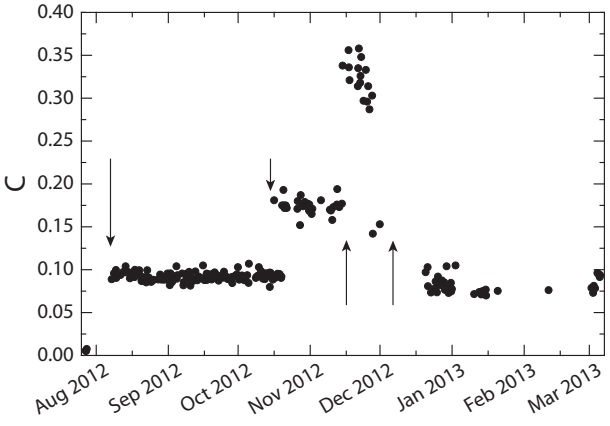

Figure 10. Time series of the routinely determined calibration constant C during measurements of Polly^{XT}_IFT from August 2012 to April 2013. Arrows denote adjustments of the neutral-density filters. The variability of C can attributed to the signal noise during the individual calibration measurements. Gaps in the time series are caused by measurement interruptions during bad weather.

5 Optimization of measurement range

Polly^{XT} was designed to measure primarily tropospheric aerosols which occur in their highest concentration close to the surface. Hence, certain optical design rules had to be considered. The most critical points concerned the laser beam stability and adjustment, the overlap function, and near-range performance. The latest type of Polly^{XT} is operated aboard the research vessels *Polarstern* and *Meteor* within the OCEANET project. Data coverage of the shallow marine boundary layer and the free troposphere is needed for studying dust fluxes, the exchange processes between the planetary boundary layer (PBL) and the free troposphere, and for comparison with ground-based in situ measurements. There-

Table 5. Beam expander of Polly. The first lens is from stock (Thorlabs, LF4938). The 2 inch lens pair is customized.

Lens type	Material	Surface radius (mm)	Thickness (mm)	Diameter (mm)
Meniscus	F. silica	150.0; 35.0	3.0	25.4
Air space			549.2	
Biconvex	CaF_2	−529.4; 157.0	7.0	50.8
Air space			7.5	
Meniscus	N-BAK2	157.0; 397.5	3.7	50.8

fore, measurements are desired from 100 m height up to the tropopause in the marine environment.

5.1 Beam expansion and overlap adjustment

Beam expansion is performed to increase the pointing stability and to reduce the divergence of the laser beam which was specified to be < 1.5 mrad. For Polly^{XT} the 7 mm beam of the Inlite-III laser is expanded to 45 mm (factor of approximately 6.5) by a single achromatic beam expander after SHG and THG (E5 in Fig. 3), which reduces the full-angle laser beam divergence to < 0.2 mrad. This value is sufficiently small with respect to the field of view of the receiver telescope of 1.0 mrad. The beam expander consists of three different lens materials for chromatic and spherical correction at the three wavelengths. The design was achieved by optimization calculation with the optical-design software ZEMAX and is given in Table 5.

In the setup of the lidar, remote overlap adjustment can be performed with the beam expander, too. The beam can be aligned by transversely shifting the achromatic lens pair (objective) of the beam expander by using two stepper motors (Engelmann and Althausen, 2014). ZEMAX calculations showed that the beam can be tilted by 3–5 mrad without reducing the beam quality, i.e., without increasing the beam divergence above 0.2 mrad. This way, no further optical steering elements have to be placed after the beam expander.

5.2 Overlap function

Tropospheric aerosol observations with lidar shall provide profiles of the extinction coefficient from the PBL to the tropopause. At low altitudes the measured signals are corrupted until the overlap function becomes unity.

In contrast, the height of complete overlap cannot be arbitrarily low because of the strong dynamic increase of the signal towards the ground (with $1/r^2$ for a range r) which cannot be covered by the detectors and data acquisition. From EARLINET workshops in previous years it emerged that such a compromise to cover measurements in the entire troposphere with only one receiver telescope is almost impossible. Therefore, it became common practice to operate different receiver telescopes for different altitude ranges. Considering the requirements for a compact and easy-to-transport lidar system, an additional near-range telescope has been included in the latest design of Polly^{XT} (see Sect. 5.3). The far-range and primary receiver of the system was designed in such a way that the overlap function of the telescope reaches unity at 800–900 m, while signals up to 20 km can be received so that the whole troposphere is covered and calibration in the Rayleigh regime (Freudenthaler, 2009a; Baars et al., 2016) is possible.

For measurements of quantities that are determined from signal ratios (backscatter coefficient by Raman method, linear depolarization, water-vapor mixing ratio) the height of complete overlap is not as essential as the equality of the overlap function for the separate detection channels. Therefore, the optical paths behind the field stop were designed in such a way that the spread of incident angles of the radiation is below 0.6° at the interference filters so that a height-independent transmission is assured (e.g., Reichardt et al., 2012). Also, the primary mirror is optically imaged onto the photocathodes of the PMTs to prevent height-dependent receiver efficiencies because of detector–surface inhomogeneities (Freudenthaler, 2004).

5.3 Near-range receiver

In order to fulfill the near-range profiling requirements with Polly^{XT}, a separate 50 mm refracting telescope was included in the design at a close distance of 98 mm from the axis of the laser beam. The conducted near-range observations can be used independently for the lidar data analysis, but provide another chance for data quality control and overlap determination of the far-range receiver as well. The refracting telescope consists of an achromatic lens (Thorlabs, AC508-250-A) with a focal length of 250 mm. A 550 µm fiber (numerical aperture 0.22) forms the field stop and transports the light. The field of view of the near-range receiver is 2.2 mrad, and the region of complete overlap was calculated by simulations to be at approximately 120 m. A fiber-optic scrambler using a Fourier lens (Arshinov et al., 2004) has been included in order to remove range-dependent angular distributions of the light when it exits the fiber and passes the adjacent beam separation and interference filters. The scrambler consists of a sapphire ball lens[3] of 2 mm diameter which directly links two fiber patch cables (Thorlabs, M37L02). Afterwards, the light passes a dichroic beam splitter and neutral-density and interference filters before the signals are detected at 532 and 607 nm.

Figure 11 shows the simulated and experimentally determined (iterative approach in Wandinger and Ansmann, 2002) overlap functions for the far-range and near-range receiving telescopes. The simulation was performed with help of the software ZEMAX. The optical geometry of the receiver was implemented in the ZEMAX model. The height-depended location and size of a laser-illuminated source plane was cal-

[3]proposed by Ilya Serikov, MPI Hamburg, Germany, 2012

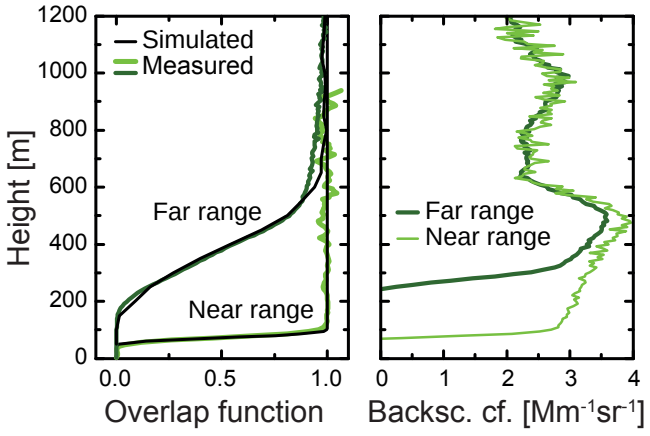

Figure 11. Left: simulated (thin, black) and experimentally determined (thick, green) overlap functions of far-range and near-range telescopes of Polly^{XT}_OCEANET. Right: Backscatter coefficient at 532 nm derived with the Klett method (lidar ratio: 30 sr, no overlap correction performed) from far-range (thick, dark green) and near-range (thin, light green) signal from a measurement aboard RV *Meteor* on 5 May 2013 form 22:00–22:30 UTC.

culated and the overlap function was determined by Ray-tracing from this plane towards the detector surface. Special coating effects (at mirrors, lenses, and interference filters) and the effect of spatially non-homogeneous photo cathodes of the PMTs were neglected for the simulation. A tilt of the laser beam towards the telescope axis of 0.3 mrad was assumed. Simulation and experimental results agree and thus show a good alignment of the system. It remains unclear where the discrepancy of 5 % of the simulated and measured far-range overlap functions above 600 m height originates. Technically, it could be caused by a slightly de-focused telescope. But due to the precise alignment procedure of the field-stop diaphragm (focal-position accuracy ±0.2 mm), it is more likely caused either by a wrong assumption of the lidar ratio during the experimental measurement of the overlap function or by a different alignment of the laser-beam angle with respect to the telescope axis than used in the simulation (0.3 mrad). Further investigation might be needed.

The particle backscatter coefficient at 532 nm is also shown for the far and near range. The correction of the overlap function was not performed in order to show the measurement differences arising from the two telescopes.

6 Case study onboard of RV *Meteor*

A detailed analysis of all optical parameters which can be retrieved with Polly^{XT}_OCEANET is presented in Fig. 12. In May 2013, the German research vessel Meteor performed an Atlantic transect cruise at 14.5° N from the Caribbean island of Guadeloupe to the Cape Verde island of São Vicente. The lidar was operated continuously during the cruise in order to study Saharan dust during its transport westward to Central America (Kanitz et al., 2014). On 9 May 2013 about 3000 km from the west African coast (14.5° N, 44.1° W) the first Saharan dust plume was observed. The layer extended from 1.7 to 3.4 km height with maximum extinction coefficients of 80 and 75 Mm^{-1} at 355 and 532 nm, respectively. The aerosol optical depth of the dust layer was approximately 0.07 ± 0.01 at 532 nm.

Polly allows us to measure particle backscatter coefficients at three wavelengths (Fig. 12a) and the corresponding backscatter-related Ångström exponents (Ångström, 1964) with very high vertical resolution. The backscatter-related Ångström exponents describe the spectral dependence of the backscatter coefficients (Fig. 12d, thick blue and red curves). Furthermore, the climate-relevant particle extinction coefficients at 355 and 532 nm are determined with the Raman lidar method (Ansmann et al., 1992; Ansmann and Müller., 2005) as well as the corresponding extinction-related Ångström exponent (Fig. 12d, thin blue curve). From the 355 and 532 nm backscatter and extinction coefficients the extinction-to-backscatter ratios (lidar ratios) are computed (shown in Fig. 12c). Together with the particle depolarization ratios in Fig. 12e and the Ångström exponents in Fig. 12d, the lidar ratios serve as a basis for an unambiguous aerosol typing (Müller et al., 2007; Tesche et al., 2011; Burton et al., 2012; Groß et al., 2013).

Lidar ratios of 50 ± 5 (for 355 nm) and 39 ± 5 sr (for 532 nm) in the lofted dust plume at 2–3 km height together with particle linear depolarization ratios of 0.16 ± 0.02 and 0.175 ± 0.01 at 355 and 532 nm, respectively, and extinction-related Ångström exponents of 0.65 ± 0.2 indicate an aged dust plume mixed with biomass-burning aerosol originating from fires in the African tropical belt (Tesche et al., 2011; Ansmann et al., 2009). Pure Saharan dust plumes caused extinction-related Ångström exponents of 0.0 ± 0.2 after Tesche et al. (2009). The interpretation of the backscatter-related Ångström exponents is complicated by the fact that dust particles are irregularly shaped and shape-related optical effects are different for different wavelengths (Gasteiger et al., 2011). However, in combination with the other optical parameters we conclude that the low backscatter-related 355/532 nm Ångström exponents of -0.01 ± 0.17 indicate comparably large smoke particles mixed with dust. According to Müller et al. (2007), smoke particles grow during transport by water uptake.

The aged lofted plume is well mixed (after the transport of 3000–5000 km from Africa according to backward trajectories) as the almost height-independent water-vapor mixing ratio (Fig. 12f) indicates. For the relative humidity we obtained values of 40 % at 2 km height up to 60 % at 3 km from radiosondes launched aboard *Meteor* which again indicates a continental African origin of the air mass.

Below the pronounced dust/smoke plume, the surface-near layer contains a mixture of dust (turbulent downward mixing and sedimentation), aged smoke, and marine par-

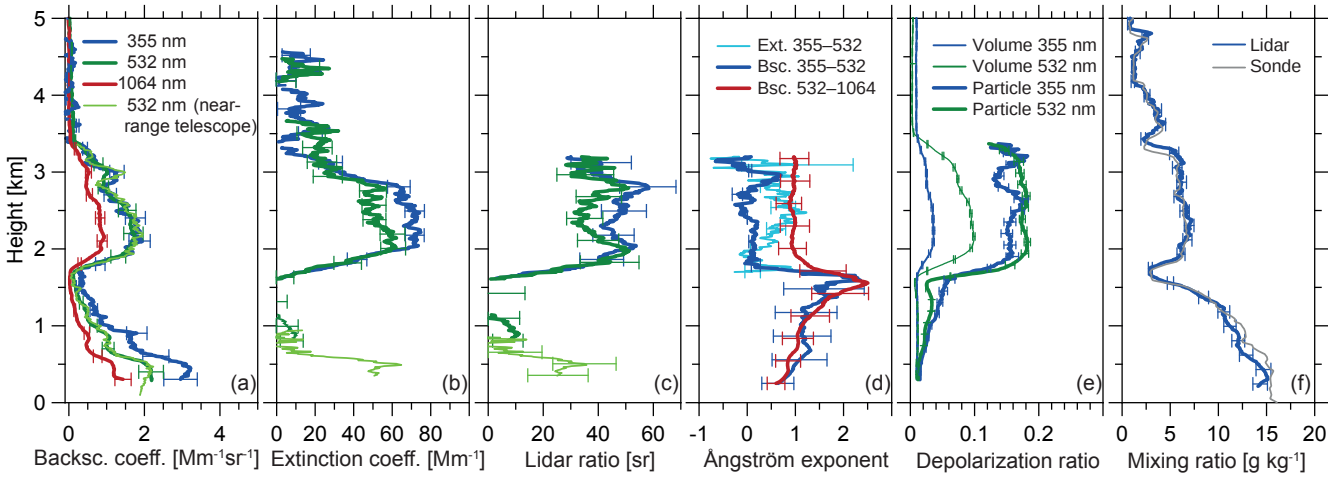

Figure 12. Optical and meteorological products obtained on board of RV *Meteor* between 23:15 and 23:58 UTC on 9 May 2013. A Saharan dust plume above the marine boundary layer was tracked. Shown are from left to right the particle backscatter coefficient, the particle extinction coefficient, the corresponding lidar ratios and Ångström exponents, the volume and particle linear depolarization ratios, and the water-vapor mixing ratio. The error bars for the water vapor, the extinction, and backscatter coefficients include the signal-noise and for the latter one also the Rayleigh-calibration errors. Those errors propagate to lidar ratio and Ångström exponent. The error bars of the depolarization ratio additionally include the calibration error of C, the uncertainties of R_i, and for the particle depolarization also the uncertainty of the backscatter coefficient.

ticles. Spherical particles (marine and smoke) dominated here and cause a particle linear depolarization ratio of $<$ 0.05 at heights below 1 km. Comparably low lidar ratios of 20 ± 10 sr and Ångström exponents around 1 also indicate a mixture of these particle components. The water-vapor mixing ratio is almost height independent in the lowest 500 m, where also the 532 nm backscatter coefficient (from near-range and far-range channels) indicates well-mixed conditions, but decreases with height as a result of mixing of drier free-tropospheric with humid boundary-layer air.

A detailed analysis of the two-wavelength depolarization-ratio profiles will allow us to quantify the contribution of marine particles, smoke, fine-mode and coarse-mode dust to the observed optical properties (Mamouri and Ansmann, 2014). The *Meteor* cruise lasted from 28 April to 23 May 2013. Based on measurements shown in Fig. 12, a detailed characterization of dust/smoke/marine particle plumes in terms of optical and derived microphysical particle properties will be performed and afterwards compared to products obtained with atmospheric circulation models. Kanitz et al. (2014) showed first intercomparisons of an ongoing analysis.

7 Current developments and outlook

In the last decade, a simple Raman lidar prototype was further developed to a mature, automated multiwavelength Raman and polarization lidar with two receiver units and $3+2+2+2+1$ capabilities (backscatter, extinction, depolarization, near-range telescope, and water vapor). The system combines latest EARLINET lidar quality standards in a stand-alone design. Until now, nine Polly systems exist. Two additional systems will be built for TROPOS in the near future. One will supplement our mobile LACROS facility and the second lidar will be permanently installed at the Cape Verde Atmospheric Observatory, Mindelo.

The constant distribution of the idea of Polly may result in a small network of lidar stations around the world with unified systems and unified data analysis along the line of the Aerosol Robotic Network (AERONET). Up to now, all Polly measurements are collected within PollyNET and quicklooks of the data products are available for the scientific community and the general public in near-real time (http://polly.tropos.de). Going even a step further, aerosol transport models can be potentially validated online or even assimilate the data and benefit from PollyNET. Furthermore, the data can be used for ground truthing of current and upcoming satellite missions.

The Polly systems have been continuously improved over the last 10 years and the progress is ongoing. Current ideas include a variety of quality-improving setup changes. For example, it is planned to automate the telecover test (Freudenthaler, 2008) and implement this test in the measurement schedule. In addition, the system is applied more and more for the investigation of aerosol-cloud interactions. An interesting approach with lidar was presented by Schmidt et al. (2013), called the dual-field-of-view technique, which might be installed in a Polly as well. Also doubling the number of photomultipliers to adjust the photon count rates for the weak aerosol backscatter on the one hand and for the strong backscatter of cloud particles on the other hand will be at-

tempted. Our colleagues from the University of Warsaw want to expand the near-range measurements to four channels to investigate the spectral behavior of absorbing aerosols in the planetary boundary layer and to enhance the overlap between ground-based remote sensing and in situ measurements. The network of fully autonomous Polly systems with its near-real-time observing capabilities is expected to play an increasing role in the establishment of a long-term, sustainable research infrastructure for aerosol and cloud profiling in the framework of ACTRIS.

Data availability

All raw data measured from PollyNET systems are automatically transferred to a public server (http://polly.tropos.de) where data quick looks are generated and displayed on a near real-time basis. In addition, profiles of backscatter and extinction coefficient and of the depolarization ratio are calculated by an automated algorithm and are presented in a graphical form (Baars et al., 2016). However, careful interpretation of automatically generated data is advised. For more information on data availability, interpretation, and on data policy please contact the responsible station principal investigator and the website.

Acknowledgements. We are deeply grateful to Volker Freudenthaler, who spends endless working hours to unify and improve the quality of lidar systems in EARLINET, for the outstanding collaboration. We also want to thank our collaboration partners for their confidence in our work and for their positive feedback. No Polly would exist without the outstanding effort of the TROPOS workshops and administration, first of all Conny Kurze and Ingolf Bernhardt. The research leading to these results has received funding from ACTRIS in the the European Union Seventh Framework Programme (FP7/2007-2013) under grant agreement no. 262254, from ACTRIS-2 in HORIZON 2020 under grant agreement no. 654109, from the Gottfried Willhelm Leibniz Association (OCEANET project in the framework of PAKT), and in the framework of BEYOND (funded under: FP7-REGPOT-2012-2013-1) under grant agreement no. 316210.

Edited by: M. Rapp

References

Althausen, D., Engelmann, R., Baars, H., Heese, B., Ansmann, A., Müller, D., and Komppula, M.: Portable Raman lidar Polly^{XT} for automated profiling of aerosol backscatter, extinction, and depolarization, J. Atmos. Ocean. Tech., 26, 2366–2378, doi:10.1175/2009JTECHA1304.1, 2009.

Althausen, D., Engelmann, E., Baars, H., Heese, B., Kanitz, T., Komppula, M., Giannakaki, E., Pfüller, A., Silva, A. M., Preißler, J., Wagner, F., Rascado, J. L., Pereira, S., Lim, J. H., Ahn, J. Y., Tesche, M., and Stachlewska, I. S.: PollyNET – a network of multiwavelength polarization Raman lidars, in: Proc. SPIE 8894, Lidar Technologies, Techniques, and Measurements for Atmospheric Remote Sensing IX, 88940I, 22 October 2013, Dresden, Germany, 8894, doi:10.1117/12.2028921, 2013.

Ångström, A.: The parameters of atmospheric turbidity, Tellus, 16, 64–75, doi:10.1111/j.2153-3490.1964.tb00144.x, 1964.

Ansmann, A. and Müller, D.: Lidar and atmospheric aerosol particles, in: Lidar – Range-Resolved Optical Remote Sensing of the Atmosphere, edited by: Weitkamp, C., Springer Series in Optical Sciences, New York, 105–141, doi:10.1007/0-387-25101-4_4, 2005.

Ansmann, A., Wandinger, U., Riebesell, M., Weitkamp, C., and Michaelis, W.: Independent measurement of extinction and backscatter profiles in cirrus clouds by using a combined Raman elastic-backscatter lidar, Appl. Optics, 31, 7113–7131, doi:10.1364/AO.31.007113, 1992.

Ansmann, A., Baars, H., Tesche, M., Müller, D., Althausen, D., Engelmann, R., Pauliquevis, T., and Artaxo, P.: Dust and smoke transport from Africa to South America: lidar profiling over Cape Verde and the Amazon rainforest, Geophys. Res. Lett., 36, L11802, doi:10.1029/2009GL037923, 2009.

Ansmann, A., Tesche, M., Groß, S., Freudenthaler, V., Seifert, P., Hiebsch, A., Schmidt, J., Wandinger, U., Mattis, I., Müller, D., and Wiegner, M.: The 16 April 2010 major volcanic ash plume over central Europe: EARLINET lidar and AERONET photometer observations at Leipzig and Munich, Germany, Geophys Res. Lett., 371, L13810, doi:10.1029/2010GL043809, 2010.

Ansmann, A., Tesche, M., Seifert, P., Groß, S., Freudenthaler, V., Apituley, A., Wilson, K. M., Serikov, I., Linné, H., Heinold, B., Hiebsch, A., Schnell, F., Schmidt, J., Mattis, I., Wandinger, U., and Wiegner, M.: Ash and fine-mode particle mass profiles from EARLINET-AERONET observations over central Europe after the eruptions of the Eyjafjallajökull volcano in 2010, Geophys. Res. Lett., 116, D00U02, doi:10.1029/2010JD015567, 2011.

Arshinov, Y., Bobrovnikov, S., Serikov, I., Althausen, D., Ansmann, A., and Mattis, I.: Optic-fiber scramblers and a fourier transform lens as a means to tackle the problem on the overlap factor of LIDAR, in: 22nd Internation Laser Radar Conference (ILRC 2004). Proceedings of the Conference held 12–16 July, 2004 in Matera, Italy, edited by: Pappalardo, G. and Amodeo, A., ESA SP-561, European Space Agency, Paris, 227–230, 2004.

Baars, H., Ansmann, A., Althausen, D., Engelmann, R., Artaxo, P., Pauliquevis, T., and Souza, R.: Further evidence for significant smoke transport from Africa to Amazonia, Geophys. Res. Lett., 382, L20802, doi:10.1029/2011GL049200, 2011.

Baars, H., Ansmann, A., Althausen, D., Engelmann, R., Heese, B., Müller, D., Artaxo, P., Paixao, M., Pauliquevis, T. M., and Souza, R.: Aerosol profiling with lidar in the Amazon Basin during the wet and dry season, J. Geophys. Res., 117, D21201, doi:10.1029/2012JD018338, 2012.

Baars, H., Kanitz, T., Engelmann, R., Althausen, D., Heese, B., Komppula, M., Preißler, J., Tesche, M., Ansmann, A., Wandinger, U., Lim, J.-H., Ahn, J. Y., Stachlewska, I. S., Amiridis, V., Marinou, E., Seifert, P., Hofer, J., Skupin, A., Schneider, F., Bohlmann, S., Foth, A., Bley, S., Pfüller, A., Giannakaki, E., Lihavainen, H., Viisanen, Y., Hooda, R. K., Pereira, S., Bortoli, D., Wagner, F., Mattis, I., Janicka, L., Markowicz, K. M., Achtert, P., Artaxo, P., Pauliquevis, T., Souza, R. A. F., Sharma, V. P., van Zyl, P. G., Beukes, J. P., Sun, J., Rohwer, E. G., Deng, R., Mamouri, R. E., and Zamorano, F.: An overview

of the first decade of Polly^{NET}: an emerging network of automated Raman-polarization lidars for continuous aerosol profiling, Atmos. Chem. Phys., 16, 5111–5137, doi:10.5194/acp-16-5111-2016, 2016.

Behrendt, A. and Nakamura, T.: Calculation of the calibration constant of polarization lidar and its dependency on atmospheric temperature, Opt. Express, 10, 805–817, 2002.

Belegante, L., Bravo-Aranda, J. A., Freudenthaler, V., Nicolae, D., Nemuc, A., Alados-Arboledas, L., Amodeo, A., Pappalardo, G., D'Amico, G., Engelmann, R., Baars, H., Wandinger, U., Papayannis, A., Kokkalis, P., and Pereira, S. N.: Experimental assessment of the lidar polarizing sensitivity, Atmos. Meas. Tech. Discuss., doi:10.5194/amt-2015-337, in review, 2016.

Böckmann, C., Wandinger, U., Ansmann, A., Bösenberg, J., Amiridis, V., Boselli, A., Delaval, A., De Tomasi, F., Frioud, M., Grigorov, I. V., Hågård, A., Horvat, M., Iarlori, M., Komguem, L., Kreipl, S., Larchevêque, G., Matthias, V., Papayannis, A., Pappalardo, G., Rocadenbosch, F., Rodrigues, J. A., Schneider, J., Shcherbakov, V., and Wiegner, M.: Aerosol lidar intercomparison in the framework of the EARLINET project. 2. Aerosol backscatter algorithms, Appl. Optics, 43, 977–989, 2004.

Bösenberg, J. and Hoff, R.: Plan for the implementation of the GAW aerosol lidar observation network GALION, World Meteorological Organization Rep., Hamburg, Germany, 178, 53 pp., 2008.

Burton, S. P., Ferrare, R. A., Hostetler, C. A., Hair, J. W., Rogers, R. R., Obland, M. D., Butler, C. F., Cook, A. L., Harper, D. B., and Froyd, K. D.: Aerosol classification using airborne High Spectral Resolution Lidar measurements – methodology and examples, Atmos. Meas. Tech., 5, 73–98, doi:10.5194/amt-5-73-2012, 2012.

D'Amico, G., Amodeo, A., Baars, H., Binietoglou, I., Freudenthaler, V., Mattis, I., Wandinger, U., and Pappalardo, G.: EARLINET Single Calculus Chain – overview on methodology and strategy, Atmos. Meas. Tech., 8, 4891–4916, doi:10.5194/amt-8-4891-2015, 2015.

D'Amico, G., Amodeo, A., Mattis, I., Freudenthaler, V., and Pappalardo, G.: EARLINET Single Calculus Chain – technical – Part 1: Pre-processing of raw lidar data, Atmos. Meas. Tech., 9, 491–507, doi:10.5194/amt-9-491-2016, 2016.

Donovan, D. P., Whiteway, J. A., and Carswell, A. I.: Correction for nonlinear photon-counting effects in lidar systems, Appl. Optics, 32, 6742–6753, doi:10.1364/AO.32.006742, 1993.

Duck, T., Firanski, B., Lind, F., and Sipler, D.: Aircraft-protection radar for use with atmospheric lidars, Appl. Optics, 44, 4937–4945, doi:10.1364/AO.44.004937, 2005.

Engelmann, R. and Althausen, D.: Lidar system including an optical device with a transmitter and a receiver, EU Patent EP2172790 B1, EPAB European Patent Applications and Specifications, Munich, Germany, 2014.

Flentje, H., Heese, B., Reichardt, J., and Thomas, W.: Aerosol profiling using the ceilometer network of the German Meteorological Service, Atmos. Meas. Tech. Discuss., 3, 3643–3673, doi:10.5194/amtd-3-3643-2010, 2010.

Foth, A., Baars, H., Di Girolamo, P., and Pospichal, B.: Water vapour profiles from Raman lidar automatically calibrated by microwave radiometer data during HOPE, Atmos. Chem. Phys., 15, 7753–7763, doi:10.5194/acp-15-7753-2015, 2015.

Freudenthaler, V.: Effects of spatially inhomogeneous photomultiplier sensitivity on LIDAR signals and remedies, in: Proceedings of the 22nd International Laser Radar Conference (ILRC 2004) held 12–16 July, 2004 in Matera, Italy, edited by: Pappalardo, G. and Amodeo, A., European Space Agency, Paris, 37 pp., ESA SP-561, 2004.

Freudenthaler, V.: The telecover test: a quality assurance tool for the optical part of a lidar system, in: Reviewed and Revised Papers Presented at the 24th International Laser Radar Conference, Boulder, Colorado, USA, 23–27 June 2008, Boulder, Colorado, USA, presentation: S01P-30, available at: http://epub.ub.uni-muenchen.de/12958/ (last access: 20 April 2015), 2008.

Freudenthaler, V.: Lidar Rayleigh-fit criteria, in: EARLINET-ASOS 7th Workshop, 09–11 February, Madrid, Spain, available at: https://epub.ub.uni-muenchen.de/12970 (last access: 19 February 2016), 2009a.

Freudenthaler, V., Esselborn, M., Wiegner, M., Heese, B., Tesche, M., Ansmann, A., Müller, D., Althausen, D., Wirth, M., Fix, A., Ehret, G., Knippertz, P., Toledano, C., Gasteiger, J., Garhammer, M., and Seefeldner, M.: Depolarization ratio profiling at several wavelengths in pure Saharan dust during SAMUM 2006, Tellus B, 61, 165–179, doi:10.1111/j.1600-0889.2008.00396.x, 2009b.

Freudenthaler, V., Groß, S., Engelmann, R., Mattis, I., Wandinger, U., Pappalardo, G., Amodeo, A., Giunta, A., D'Amico, G., Chaikovsky, A., Osipenko, F., Slesar, A., Nicolae, D., Belegante, L., Talianu, C., Serikov, I., Linne, H., Jansen, F., Wilson, K., de Graaf, M., Apituley, A., Trickl, T., Giehl, H., and Adam, M.: EARLI09 – direct intercomparison of eleven EARLINET lidar systems, in: Proceedings of the 25th International Laser Radar Conference, 5–9 July 2010, St.-Petersburg, Russia, ISBN: 978-5-94458-109-9, 891–894, 2010.

Freudenthaler, V.: About the effects of polarising optics on lidar signals and the Δ90-calibration, Atmos. Meas. Tech. Discuss., doi:10.5194/amt-2015-338, in review, 2016.

Gasteiger, J., Wiegner, M., Groß, S., Freudenthaler, V., Toledano, C., Tesche, M., and Kandler, K.: Modelling lidar-relevant optical properties of complex mineral dust aerosols, Tellus B, 63, 725–741, doi:10.1111/j.1600-0889.2011.00559.x, 2011.

Groß, S., Esselborn, M., Weinzierl, B., Wirth, M., Fix, A., and Petzold, A.: Aerosol classification by airborne high spectral resolution lidar observations, Atmos. Chem. Phys., 13, 2487–2505, doi:10.5194/acp-13-2487-2013, 2013.

Johnson, F. A., Jones, R., McLean, T. P., and Pike, E. R.: Dead-time corrections to photon counting distributions, Phys. Rev. Lett., 16, 589–592, doi:10.1103/PhysRevLett.16.589, 1966.

Kanitz, T., Seifert, P., Ansmann, A., Engelmann, R., Althausen, D., Casiccia, C., and Rohwer, E. G.: Contrasting the impact of aerosols at northern and southern midlatitudes on heterogeneous ice formation, Geophys. Res. Lett., 38, L17802, doi:10.1029/2011GL048532, 2011.

Kanitz, T., Ansmann, A., Engelmann, R., and Althausen, D.: North-south cross sections of aerosol layering over the Atlantic Ocean from multiwavelength Raman/polarization lidar during Polarstern cruises, J. Geophys. Res., 118, 2642–2655, doi:10.1002/jgrd.50273, 2013.

Kanitz, T., Engelmann, R., Heinold, B., Skupin, A., and Ansmann, A.: Tracking the Saharan Air Layer with shipborne lidar across the tropical Atlantic, Geophys. Res. Lett., 41, 1044–1050, doi:10.1002/2013GL058780, 2014.

Liu, Z., Kuehn, R., Vaughan, M., Winker, D., Omar, A., Powell, K., Trepte, C., Hu, Y., and Hostetler, C.: The CALIPSO cloud and aerosol discrimination: version 3 algorithm and test results, in: Proceedings of the 25th International Laser Radar Conference, 5–9 July 2010, St.-Petersburg, Russia, ISBN: 978-5-94458-109-9, 891–894, 2010.

Mamouri, R. E. and Ansmann, A.: Fine and coarse dust separation with polarization lidar, Atmos. Meas. Tech., 7, 3717–3735, doi:10.5194/amt-7-3717-2014, 2014.

Mattis, I., Ansmann, A., Althausen, D., Jaenisch, V., Wandinger, U., Müller, D., Arshinov, Y. F., Bobrovnikov, S. M., and Serikov, I. B.: Relative-humidity profiling in the troposphere with a Raman lidar, Appl. Optics, 41, 6451–6462, 2002.

Mattis, I., Tesche, M., Grein, M., Freudenthaler, V., and Müller, D.: Systematic error of lidar profiles caused by a polarization-dependent receiver transmission: quantification and error correction scheme, Appl. Optics, 48, 2741–2751, 2009.

Mattis, I., D'Amico, G., Baars, H., Amodeo, A., Madonna, F., and Iarlori, M.: EARLINET Single Calculus Chain – technical Part 2: Calculation of optical products, Atmos. Meas. Tech. Discuss., doi:10.5194/amt-2016-43, in review, 2016.

Müller, D., Wandinger, U., and Ansmann, A.: Microphysical particle parameters from extinction and backscatter lidar data by inversion with regularization: theory, Appl. Optics, 38, 2346–2357, doi:10.1364/AO.38.002346, 1999.

Müller, D., Ansmann, A., Mattis, I., Tesche, M., Wandinger, U., Althausen, D., and Pisani, G.: Aerosol-type-dependent lidar ratios observed with Raman lidar, J. Geophys. Res., 112, D16202, doi:10.1029/2006JD008292, 2007.

Omar, A. H., Winker, D. M., Kittaka, C., Vaughan, M. A., Liu, Z., Hu, Y., Trepte, C. R., Rogers, R. R., Ferrare, R. A., Lee, K. P., Kuehn, R. E., and Hostetler, C. A.: The CALIPSO automated aerosol classification and lidar ratio selection algorithm, J. Atmos. Ocean. Tech., 26, 1994–2014, doi:10.1175/2009JTECHA1231.1, 2009.

Pappalardo, G., Amodeo, A., Pandolfi, M., Wandinger, U., Ansmann, A., Bösenberg, J., Matthias, V., Amiridis, V., De Tomasi, F., Frioud, M., Iarlori, M., Komguem, L., Papayannis, A., Rocadenbosch, F., and Wang, X.: Aerosol lidar intercomparison in the framework of the EARLINET project. 3. Raman lidar algorithm for aerosol extinction, backscatter, and lidar ratio, Appl. Optics, 43, 5370–5385, doi:10.1364/AO.43.005370, 2004.

Pappalardo, G., Amodeo, A., Apituley, A., Comeron, A., Freudenthaler, V., Linné, H., Ansmann, A., Bösenberg, J., D'Amico, G., Mattis, I., Mona, L., Wandinger, U., Amiridis, V., Alados-Arboledas, L., Nicolae, D., and Wiegner, M.: EARLINET: towards an advanced sustainable European aerosol lidar network, Atmos. Meas. Tech., 7, 2389–2409, doi:10.5194/amt-7-2389-2014, 2014.

PollyNET: Worldwide observations with the portable Raman lidar systems (Polly), available at: http://polly.tropos.de, 2016.

Preißler, J., Wagner, F., Guerrero-Rascado, J. L., and Silva, A. M.: Two years of free-tropospheric aerosol layers observed over Portugal by lidar, J. Geophys. Res., 118, 3676–3686, doi:10.1002/jgrd.50350, 2013.

Reichardt, J., Baumgart, R., and McGee, T. J.: Three-signal method for accurate measurements of depolarization ratio with lidar, Appl. Optics, 42, 4909–4913, doi:10.1364/AO.42.004909, 2003.

Reichardt, J., Wandinger, U., Klein, V., Mattis, I., Hilber, B., and Begbie, R.: RAMSES: German Meteorological Service autonomous Raman lidar for water vapor, temperature, aerosol, and cloud measurements, Appl. Opt., 51, 8111–8131, doi:10.1364/AO.51.008111, 2012.

Sakai, T., Nagai, T., Zaizen, Y., and Mano, Y.: Backscattering linear depolarization ratio measurements of mineral, sea-salt, and ammonium sulfate particles simulated in a laboratory chamber, Appl. Optics, 49, 4441–4449, doi:10.1364/AO.49.004441, 2010.

Sassen, K.: Meteorology: dusty ice clouds over Alaska, Nature, 434, 456, doi:10.1038/434456a, 2005.

Schmidt, J., Wandinger, U., and Malinka, A.: Dual-field-of-view Raman lidar measurements for the retrieval of cloud microphysical properties, Appl. Optics, 52, 2235–2247 doi:10.1364/AO.52.002235, 2013.

Seifert, P., Ansmann, A., Mattis, I., Wandinger, U., Tesche, M., Engelmann, R., Müller, D., Pérez, C., and Haustein, K.: Saharan dust and heterogeneous ice formation: eleven years of cloud observations at a central European EARLINET site, J. Geophys. Res., 115, 2156–2202, doi:10.1029/2009JD013222, 2010.

Simeonov, V., Larcheveque, G., Quaglia, P., van den Bergh, H., and Calpini, B.: Influence of the photomultiplier tube spatial uniformity on lidar signals, Appl. Optics, 38, 5186–5190, doi:10.1364/AO.38.005186, 1999.

Tesche, M., Ansmann, A., Müller, D., Althausen, D., Engelmann, R., Freudenthaler, V., and Groß, S.: Vertically resolved separation of dust and smoke over Cape Verde using multiwavelength Raman and polarization lidars during Saharan Mineral Dust Experiment 2008, J. Geophys. Res., 114, D13202, doi:10.1029/2009JD011862, 2009.

Tesche, M., Groß, S., Ansmann, A., Müller, D., Althausen, D., Freudenthaler, V., and Esselborn, M.: Profiling of Saharan dust and biomass-burning smoke with multiwavelength polarization Raman lidar at Cape Verde, Tellus B, 63, 16360, doi:10.3402/tellusb.v63i4.16360, 2011.

Tesche, M., Glantz, P., Johansson, C., Norman, M. G., Hiebsch, A., Seifert, P., Ansmann, A., Engelmann, R., and Althausen, D.: Volcanic ash over Scandinavia originating from the Grimsvötn eruptions in May 2011, J. Geophys. Res., 117, D09201, doi:10.1029/2011JD017090, 2012.

Wandinger, U.: Raman Lidar, in: Lidar – Range-Resolved Optical Remote Sensing of the Atmosphere, edited by: Weitkamp, C., Springer Series in Optical Sciences, New York, 241–271, doi:10.1007/0-387-25101-4_9, 2005.

Wandinger, U. and Ansmann, A.: Experimental determination of the lidar overlap profile with Raman lidar, Appl. Optics, 41, 511–514, 2002.

Wandinger, U., Seifert, P., Engelmann, R., Bühl, J., Wagner, J., Schmidt, J., Pospichal, B., Baars, H., Hiebsch, A., Kanitz, T., Skupin, A., Pfitzenmaier, L., Heese, B., Althausen, D., and Ansmann, A.: Observations of aerosol-cloud-turbulence interaction with integrated remote-sensing instrumentation, in: Proceedings of the 9th International Symposium on Tropospheric Profiling, edited by: Cimini, D., Di Girolamo, P., Marzano, F. S., and Rizi, V., L'Aquila, Italy, 3–7 September 2012, doi:10.12898/ISTP9prc, 2012.

Wandinger, U., Freudenthaler, V., Baars, H., Amodeo, A., Engelmann, R., Mattis, I., Groß, S., Pappalardo, G., Giunta, A., D'Amico, G., Chaikovsky, A., Osipenko, F., Slesar, A., Nicolae, D., Belegante, L., Talianu, C., Serikov, I., Linné, H., Jansen, F., Apituley, A., Wilson, K. M., de Graaf, M., Trickl, T., Giehl, H., Adam, M., Comerón, A., Muñoz-Porcar, C., Rocadenbosch, F., Sicard, M., Tomás, S., Lange, D., Kumar, D., Pujadas, M., Molero, F., Fernández, A. J., Alados-Arboledas, L., Bravo-Aranda, J. A., Navas-Guzmán, F., Guerrero-Rascado, J. L., Granados-Muñoz, M. J., Preißler, J., Wagner, F., Gausa, M., Grigorov, I., Stoyanov, D., Iarlori, M., Rizi, V., Spinelli, N., Boselli, A., Wang, X., Lo Feudo, T., Perrone, M. R., De Tomasi, F., and Burlizzi, P.: EARLINET instrument intercomparison campaigns: overview on strategy and results, Atmos. Meas. Tech., 9, 1001–1023, doi:10.5194/amt-9-1001-2016, 2016.

Whiteman, D. N.: Examination of the traditional Raman lidar technique. I. Evaluating the temperature-dependent lidar equations, Appl. Optics, 42, 2571–2592, doi:10.1364/AO.42.002571, 2003.

Winker, D. M., Vaughan, M. A., Omar, A., Hu, Y., Powell, K. A., Liu, Z., Hunt, W. H., and Young, S. A.: Overview of the CALIPSO mission and CALIOP data processing algorithms, J. Atmos. Ocean. Tech., 26, 2310–2323, doi:10.1175/2009JTECHA1281.1, 2009.